Rebound of large jets from superhydrophobic surfaces in low gravity

Karl Cardin, Sheng Wang, Olivier Desjardins, and Mark Weislogel

Phys. Rev. Fluids **6**, 014003 — Published 20 January 2021

DOI: 10.1103/PhysRevFluids.6.014003

Rebound of Large Jets from Superhydrophobic Surfaces in Low-Gravity

Karl Cardin,[1,*] Sheng Wang,[2] and Mark Weislogel[1]
[1] *Portland State University*
[2] *Cornell University*
(Dated: December 9, 2020)

We experimentally investigate the phenomena of large jet rebound, a mode of fluid transfer following oblique jet impacts on superhydrophobic substrates. We initially seek to describe the jet rebound regimes in tests conducted in the weightless environment of a drop tower. A parametric study reveals the dependence of the flow structure on the relevant dimensionless groups such as Reynolds number and Weber number defined on the velocity component perpendicular to the substrate. We show that significantly larger diameter jets behave similarly as much smaller jets demonstrated during previous terrestrial investigations in some parameter ranges while the flow is fundamentally different in others. Level-set numerical predictions are provided for comparisons where practicable. Simple models are developed predicting landing geometry and the onset of instability that are found to yield good agreement with experiments and simulations. Improving our understanding of such jet rebound opens avenues for unique transport capabilities.

I. INTRODUCTION

Liquid jet impingement on solid substrates is a thoroughly studied field due to the beauty, variety, and applicability of the phenomena. The thermophysical properties of the fluid and nature of the solid substrate determines a vast array of impact structures from smooth radial films and hydraulic jumps for wetting substrates, to crowning and splashing for non-wetting liquids [1–5]. Jet impact on non-wetting substrates has remained relatively unstudied when compared to wetting cases. This investigation focuses on the flow structures resulting from oblique water jet impact with a superhydrophobic substrate in the low-gravity (low-g) environment of a drop tower where capillary and inertial forces dominate.

With reference to Fig. 1, when an oblique water jet impacts a sufficiently hydrophobic substrate the radial landing flow extension is limited by surface tension. Fluid accumulates along the landing flow edge creating relatively thick bounding rims, Fig. 1(c). As the jet-substrate impact angle ϕ_i, Fig. 1(b), decreases, the streamwise advection associated with the jet velocity component parallel to the substrate $v_{\parallel}$ stretches the landing flow downstream resulting in the leaf-shaped geometry observed in Fig. 1(a). The rims collide at the downstream apex giving rise to a rebounded jet that leaves the substrate due to vertically imbalanced forces. The non-wetting conditions of the substrate are critical to the dynamics of the process.

As for jet impact on any substrate, jet spreading, splashing, receding, and rebound are highly dependent on jet velocity, fluid properties, and incident angle culminating in a perpendicular Weber number $\mathrm{We}_\perp \equiv \rho v_\perp^2 d_j/\sigma$ and jet Reynolds number $\mathrm{Re} \equiv \rho v d_j/\mu$, where v is the jet velocity, $v_\perp$ is the jet velocity normal to the surface, ρ is the fluid density, d_j is the jet diameter, and σ is the surface tension.

Celestini *et al.* [6] demonstrate jet rebound of submillimetric jets from horizontally oriented hydrophobic substrates with apparent contact angles θ^* of 110° and 155°. From their data they construct a regime map of stable and unstable rebounds. Celestini *et al.* [6] also displayed multiple rebounds of a single jet from assemblies of planar hydrophobic substrates. Kibar *et al.* [7], Kibar [8] investigate the spreading area of the landing flow and the force exerted on a variety of vertically oriented hydrophobic substrates by rebounds of 1.75 and 4 mm diameter jets. These previous investigations focus on low velocity impact regimes where the jet rebounds without splashing. Celestini *et al.* [6] and Kibar [8] investigated a parameter space encompassing Re 100-3000, $\mathrm{We}_\perp$ 0-20 and Re 1750-3050, $\mathrm{We}_\perp$ 0-30, respectively.

This investigation includes 'large' jets with a diameter d_j greater than the capillary length $l_c \equiv (\sigma/\rho g)^{1/2}$. The capillary length is approximately 2.7 mm for water subjected to terrestrial gravity $g_o = 9.81\,\mathrm{m\,s^{-2}}$. The jet Bond number $\mathrm{Bo} \equiv d_j/l_c \ll 1$ expresses the relative importance of gravity to surface tension and is negligible for the present investigation because free fall drop tower environments routinely achieve brief effective low-gravity levels $g \lesssim 10^{-4} g_o$. By employing a drop tower, we maintain Bo << 1 while expanding Re and $\mathrm{We}_\perp$ by an order of magnitude compared to Celestini *et al.* [6].

* kcardin@pdx.edu

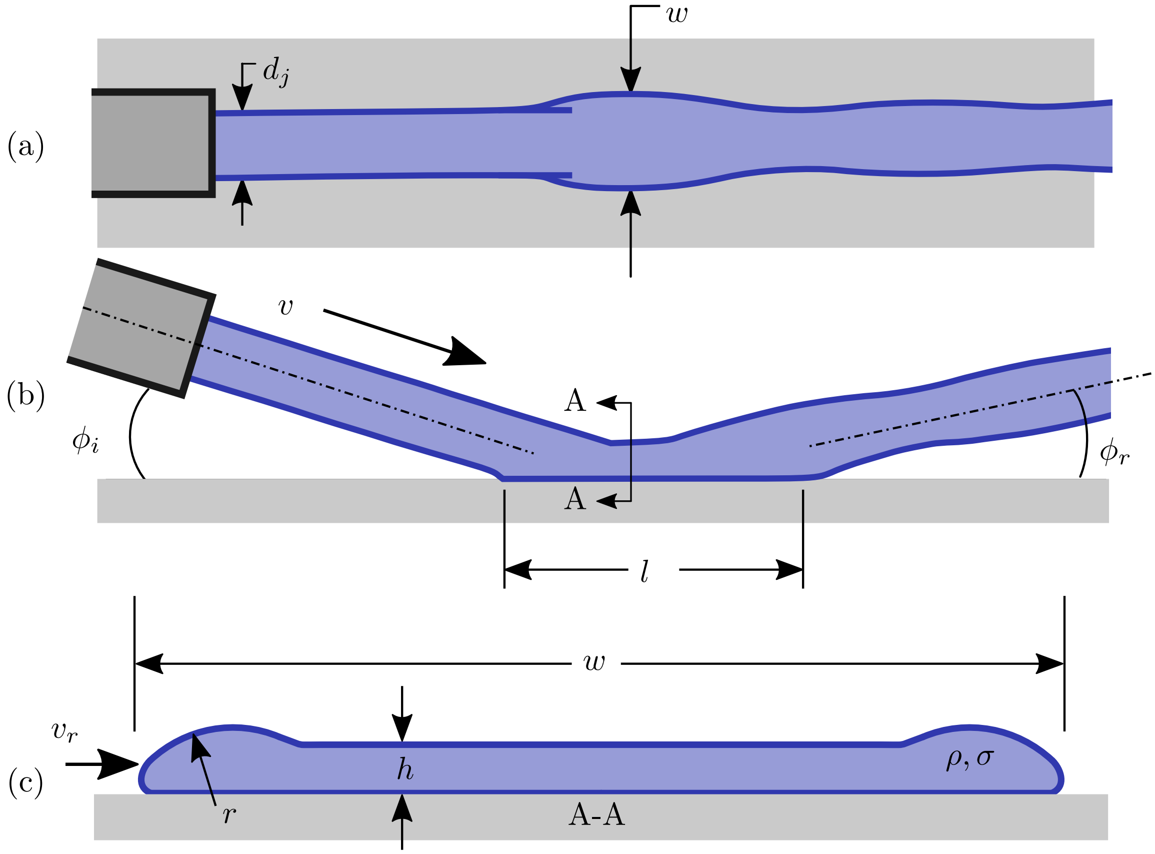

FIG. 1. Schematic of oblique jet impact with landing flow and rebound from a hydrophobic substrate: (a) top view, (b) profile view, and (c) cross-section view of the landing flow at the point of maximum width w with bounding rims identified by radius r.

Jet impingement with superhydrophobic surfaces is dynamically similar to the impingement of two jets. Bush and Hasha [9] investigate the oblique impingement of two jets in low-inertia regimes. At the smallest jet velocities the impact results in a series of mutually orthogonal leaf-shaped chains with thick bounding rims. Each downstream link of such a fluid chain reduces in size until a single deformed jet emerges. As the jet velocity increases the rim destabilizes resulting in a 'fishbone' structure characterized by an organized array of ligaments forming along the sheet edge ultimately creating droplets that eject away from the sheet. Many studies have investigated the impact of two jets at higher velocities [10, 11]. At high jet velocities ligaments begin to form along the rim, the sheet 'opens' such that there is no re-impingement, and eventually the sheet disintegrates providing a fine spray of droplets. Atomization regimes have received tremendous attention due to their practical application in fuel atomization (e.g., bipropellant rocket engines).

Understanding and controlling jet rebound dynamics, including the landing flow structure and secondary jet characteristics, is essential to its application to engineering processes. One of the critical, and yet to be determined, characteristics of these flows is the transition to a splashing regime. Insight into the landing flow dimensions is also desired. Knowledge of jet rebound mechanics can provide significant contributions to many engineering applications including open-air microfluidics, fire suppression on spacecraft, and coating processes.

The drop tower test data collected herein is employed to extend the jet rebound regime map by highlighting landing flow structure as a function of the relevant dimensionless groups Re and $\mathrm{We}_\perp$. Building on the work of Celestini *et al.* [6], we identify new regimes that further subdivide the unstable regime and add novel regimes observed in the limits of large and small impact angles. Simple approximate analytic models are developed for the rim pinching, landing flow residence time, onset of instability, and landing flow dimensions. Following a discussion of substrates, experimental apparatus, procedures, and numerical methods, we present both experimental and computational data for comparisons. The work is concluded with a summary of observations, open questions, and future work.

II. LANDING FLOW RETRACTION

During landing flow spreading, a bounding rim is established where the decreasing liquid inertia is resisted and eventually overcome by capillary pressure, leading to retraction of the landing flow after the point of maximum width w, a collision of the bounding rims, and a rebound of the jet due to the vertical asymmetry of the flow. In other words, the jet transitions towards a lower energy cylindrical state and pushes away from the substrate. Superhydrophobic surfaces provide minimal adhesion of the liquid to the substrate allowing retraction dynamics similar to a fluid surrounded by air. The minimal dissipation provided by the surface during spreading and retraction of the landing flow is essential for jet rebound.

We employ a Taylor-Culick approach commonly used for the inertial retraction of thin films to describe the rim retraction rate [12, 13]. Considering a sheet with cross-section shown in Fig. 1(c), a balance between the rate of change of rim momentum P_{rim} and the surface tension force exerted on the rim yields

$$\frac{\mathrm{d}P_{\mathrm{rim}}}{\mathrm{d}t} = v_{\mathrm{ret}}\frac{\mathrm{d}m}{\mathrm{d}t} = 2\sigma, \tag{1}$$

where v_{ret} is the constant rim speed and m is the rim mass per unit length. The rate of change of the rim mass can be expressed as

$$\frac{\mathrm{d}m}{\mathrm{d}t} = \rho h v_{\mathrm{ret}}. \tag{2}$$

Inserting Eq. 2 into Eq. 1 yields the Taylor-Culick speed

$$v_{\mathrm{ret}} = \left(\frac{2\sigma}{\rho h}\right)^{1/2} \tag{3}$$

This retraction velocity can be quantitatively confirmed by considering the convergence angle of the landing flow after the point of maximum width. Using the cross-stream velocity v_{ret} along with the downstream velocity $v_{\|}$, the convergence angle is estimated by $\beta \approx \tan^{-1}(v_{\mathrm{ret}}/v_{\|})$. This prediction for the landing flow angle shows qualitative agreement with images taken from drop tower tests as shown in Fig. 2.

For small ϕ_i, the residence time of the landed jet is largely consumed by such rim retraction towards the apex. Therefore, the landing jet residence time is approximated as

$$\tau_r \sim \frac{w}{2v_{\mathrm{ret}}} \sim \left(\frac{\rho h w^2}{8\sigma}\right)^{1/2}. \tag{4}$$

III. RIM INSTABILITY

For high Weber number impacts, varicose rim perturbations are observed near the point of impact and continue to propagate downstream. Given sufficient time such varicose perturbations lead to the breakup of the bounding rims. The wavelength of the varicose perturbations and rim radius r were measured from top view images of fishbone landing flows and the perturbation wavelength was found to be close to the most unstable wavelength for a free jet $\lambda \sim 9.01r$ [14], which supports the role of the Rayleigh-Plateau instability in the breakup of the rim. The rim radius of fishbone landing flows is found to be $\sim 2h$ by measuring the rim diameter at maximum landing flow width from top view images and equating the landing flow cross-section, assuming it is a rectangular slab bound by two half-circles, to the jet cross-section. The relevant time scale for Rayleigh-Plateau pinching and breakup τ_p is the capillary-inertial time scale

$$\tau_p \sim \left(\frac{\rho 8 h^3}{\sigma}\right)^{1/2}. \tag{5}$$

Later we will compare τ_p to the residence time τ_r to predict the onset of splashing.

A. Energy Model

It is observed that the value of w depends far more on the jet perpendicular velocity $v_\perp$ than tangential jet velocity $v_{\|}$. We conclude that the kinetic energy of the jet normal to the substrate is largely converted to excess landing flow

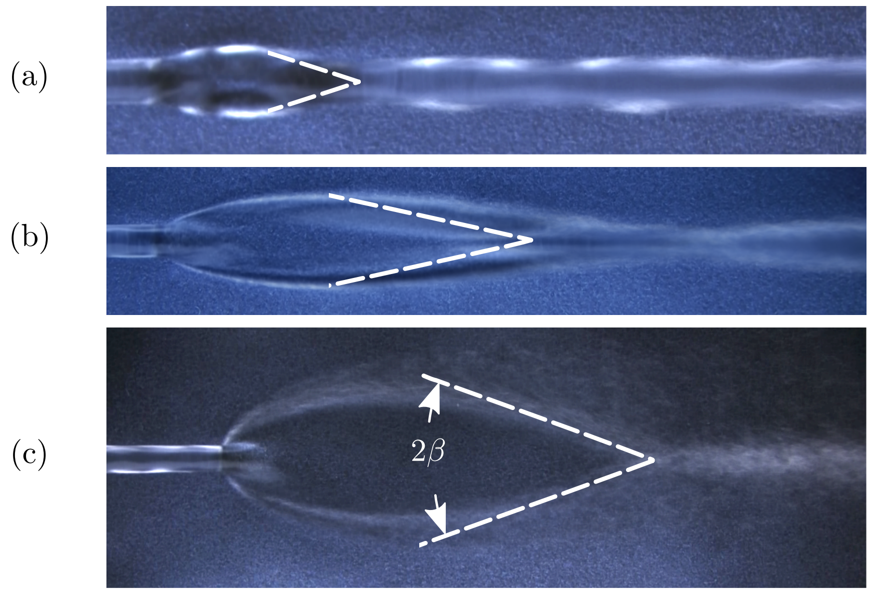

FIG. 2. Time averaged images from drop tower tests of landing flows with the predicted convergence angle β overlaid. Tests: (a) $\phi_i = 15.1°$, $\mathrm{We}_\perp = 1.50$ (D1), (b) $\phi_i = 18.3°$, $\mathrm{We}_\perp = 10.05$ (D3), and (c) $\phi_i = 33.5°$, $\mathrm{We}_\perp = 37.12$ (D4). The blurred landing flow boundary in (c) is the result of droplets leaving the landing flow rim.

surface energy. Before impact the jet is modeled as a cylinder of diameter d_j and length L traveling towards the substrate at velocity $v_\perp$ with the cylinder axis parallel to the substrate. The free jet energy is $E_1 = E_{KE,1} + E_{S,1}$, where $E_{KE,1} = \frac{1}{8}\rho\pi d_j^2 v_\perp^2 L$ is the initial kinetic energy and $E_{s,1} = \sigma_{lg}\pi d_j L$ is the initial surface energy. The per-length energy of the zero normal velocity landing flow is $E_2 = (A\sigma)_{sg} + (A\sigma)_{sl} + (A\sigma)_{lg}$ where $A\sigma$ is the surface energy of each solid-liquid (sl), solid-gas (sg), and liquid-gas (lg) interface. Equating these two energies and employing the Cassie-Baxter equation [15] $r_s f \frac{\sigma_{gs}-\sigma_{sl}}{\sigma_{lg}} - 1 + f = \cos\theta^*$, where $\cos\theta^*$ is the apparent contact angle, yields an expression for the maximum width of the landing flow

$$w = \pi d_j \frac{\frac{d_j \rho v_\perp^2}{8\sigma_{lg}} + 1}{\cos(\theta^*) - f + 1 - R_{lg}}, \tag{6}$$

where $R_{lg} = A_{lg}/w$ is the liquid-gas interface roughness [16]. Kaps *et al.* [16] chose $R_{lg} = 2$ assuming that the top and bottom liquid-gas interface areas are equal and Kibar [8] determined R_{lg} from simulations.

In this work the landing flow geometry at maximum width is modeled as a rectangular slab of height H, width W, and length L. Employing the geometric condition $HW = \pi d_j^2/4$, the liquid-gas interface roughness is $R_{lg} = \frac{\pi d_j^2}{4W^2} + 2 - f$. Inserting R_{lg} into Eq. 6 and rearranging yields a quadratic equation

$$W^2\sigma_{lg}(1-\cos(\theta^*)) + \sigma_{lg}\frac{\pi d_j^2}{2} = W\left(\frac{1}{8}\rho\pi d_j^2 v_\perp^2 + \sigma_{lg}\pi d_j\right). \tag{7}$$

The physical, positive root of Eq. 7 is

$$W = \frac{\pi d_j}{16}\frac{(\mathrm{We}_\perp + 8)}{(1-\cos\theta^*)}\left(1 + \left[1 - \frac{128(1-\cos\theta^*)}{\pi}\left(\frac{1}{\mathrm{We}_\perp + 8}\right)^2\right]^{1/2}\right). \tag{8}$$

When $\mathrm{We}_\perp >> 1$, setting $\theta^* = 180°$, solving Eq. 8 for the normalized landing flow width W/d_j gives

$$\frac{W}{d_j} = C_1 \frac{\pi(\mathrm{We}_\perp + 8)}{16}, \tag{9}$$

where the prefactor C_1 is introduced as a fit parameter to match experimental data. Equation 9 provides a simple prediction for the landing flow dimensions.

B. Splashing

As stated, a larger perpendicular Weber number $\mathrm{We}_\perp$ increases the time for the Rayleigh-Plateau instability to induce pinching along the landing flow rim. Bulbous regions of the rim draw out ligaments as the rim retracts that eventually pinch off resulting in an array of droplets in the wake of the landing flow. It is expected that the rim will become unstable when the residence time of a fluid parcel in the rim exceeds the pinching time of the rim: $\tau_r/\tau_p \gtrsim 1$. Evaluating this criteria with Eq. 4 and Eq. 5 yields

$$w\left(\frac{\rho h}{8\sigma}\right)^{1/2}\left(\frac{\sigma}{8\rho h^3}\right)^{1/2} = \frac{w}{8h} > 1. \tag{10}$$

Letting $h \sim H$, $w \sim W$, and again using the geometric property $HW = \pi d_j^2/4$, Eq. 10 becomes

$$\frac{W}{8}\frac{4W}{\pi d_j^2} > 1.$$

Instability will occur when

$$\frac{W}{d_j} > (2\pi)^{1/2}. \tag{11}$$

Inserting Eq. 9 gives

$$\mathrm{We}_\perp > \frac{16}{C_1}\left(\frac{2}{\pi}\right)^{1/2} - 8, \tag{12}$$

which provides a critical Weber number for the onset of splashing.

IV. METHODOLOGY

All experiments are performed at the Dryden Drop Tower facility at Portland State University. The Dryden Drop Tower (DDT) is a safe, low-cost, high-rate facility located in the atrium of an engineering building on campus. An image of the tower is provided in Fig. 3. During a drop test the rig and drag shield are released simultaneously; because the rig is enclosed in the drag shield, the rig is largely protected from aerodynamic drag during free fall. The drag shield and experiment rig fall 22 m providing 2.1 s of relative low-gravity g $< 10^{-4} g_o$. Additional DDT introduction details are provided by Wollman [17].

A. Apparatus

A schematic of the jet rebound experiment rig is sketched in the Fig. 4, with devices for fluid injection, jet/substrate positioning, and image capture labeled. An accumulator consisting of two rigid reservoirs separated by a flexible membrane delivers the liquid jets for all tests. The upstream reservoir is filled with air and the downstream reservoir is filled with water. When the solenoid is actuated open, the large upstream reservoir provides ideal gas expansion displacing the membrane and downstream reservoir water through the nozzle at a controlled flow rate. During each 2.1 s test the gas pressure decreases $< 5\%$ yielding undetectable changes in measurable jet characteristics such as landing flow length l. For each experiment the accumulator is filled with the test fluid followed by air until the desired pressure set point is reached.

The jet steady velocity v is determined via terrestrial calibration using a balance scale and time interval to determine the mean mass flow rate as a function of initial pressure. Jet flow rates $0.1 \leq v \leq 33.8\,\mathrm{ml\,s^{-1}}$ are established. Room temperature water is the working fluid for all tests reported with measured surface tension $\sigma = 0.0716 \pm 0.0001\,\mathrm{N\,m^{-1}}$.

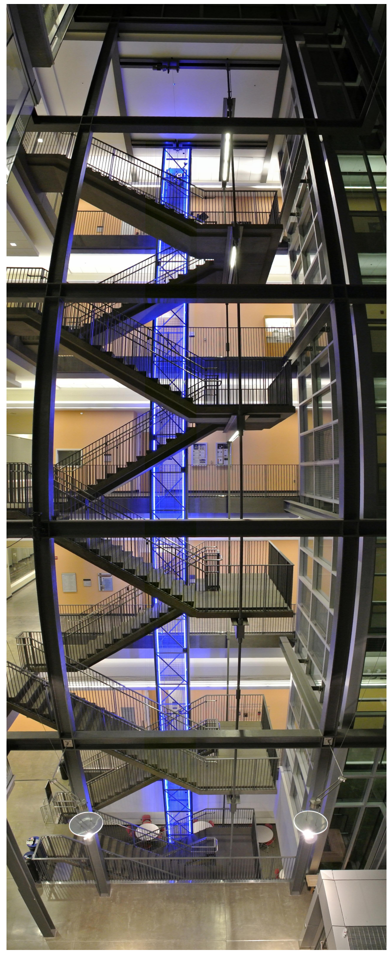

FIG. 3. Photograph of the Dryden Drop Tower at Portland State University.

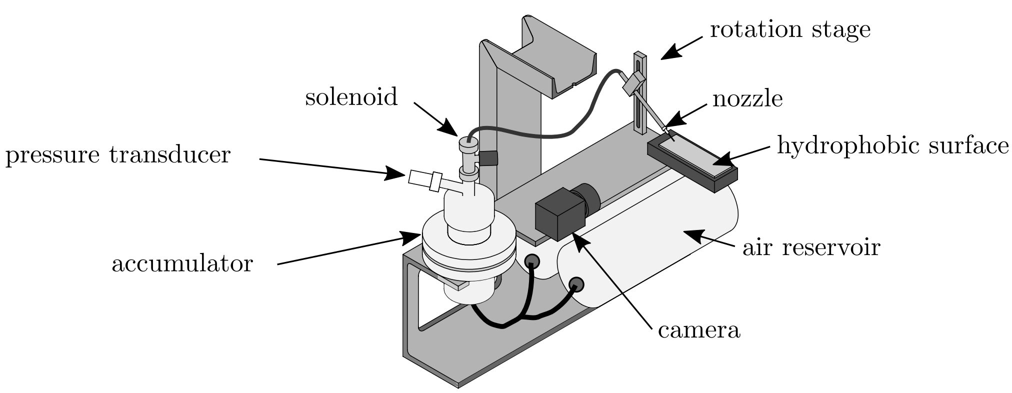

FIG. 4. Partial cutaway view of drop tower experiment rig with critical items identified.

The jet nozzles consist of either a blunt commercial stainless steel dispensing needle or a length of stainless steel tubing. Nozzle diameters d_j of 0.3, 0.5, 1.3, 1.7, 2.4, 2.9, and 6.0 mm are employed. The nozzles are mounted to a manual rotation stage allowing for easy adjustment of the jet-substrate impact angle. A representative set of drop test experiment parameters are included in Table I. A drop index D# has been assigned to each test case in the table for reference.

TABLE I. Parameters for a representative selection of drop tower tests.

Drop Index	d_j (mm)	Flow Rate (mL s^{-1})	ϕ_i (deg)	$\mathrm{We}_\perp$	w (mm)
D1	6.0	14.40	15.1	1.50	9.14
D2	0.5	1.00	15.7	12.53	0.74
D3	6.0	31.00	18.3	10.05	16.18
D4	6.0	33.80	33.5	37.12	29.16
D5	0.5	0.80	49.3	63.23	2.84

B. Superhydrophobic Substrate

A substrate is hydrophilic if $0 < \theta < 90°$, hydrophobic if $90 < \theta \leq 150°$, and superhydrophobic if $150 < \theta < 180°$. A superhydrophobic substrate is developed, in part, to support this work. The process creates uniform, repeatable, non-wetting substrates. Our method uses ISO P400 silicon carbide sandpaper bonded to a PMMA plate; the sandpaper provides the surface texture essential for superhydrophobic substrates. The sandpaper surface is then coated with a PTFE aerosol spray (King Controls: Dome Magic) to create a superhydrophobic substrate. The PTFE spray canister is held approximately 0.2 m above the substrate and sprayed in widthwise strokes with 50% overlap between adjacent strokes. Each substrate initially receives three applications of PTFE spray with subsequent periodic reapplication between tests. No notable changes in the superhydrophobic substrate characteristics are observed during drop tests. The static sessile drop contact angle for water on the substrates measures $\theta^* = 158 \pm 5°$, as determined by the *Surface Evolver* algorithm [18] via the SE-FIT user interface [19]. Additionally, advancing and receding contact angles found to be above the superhydrophobic of 150°.

C. Data Collection and Reduction

All tests are imaged at 60 or 120 fps with 1920×1080 pixel resolution from both profile and top perspectives using consumer-grade Panasonic cameras model HC-WX970 or HDC-TM900. Due to limited pixel density, especially for small jet diameters, errors in the landing flow region measurements approach 5%. A diffuse LED array is adopted to backlight the phenomena. For each test the jet is established before the release of the drop rig into free fall such that both 1-g and low-g data is recorded. The jet rebound regimes are assessed qualitatively from the video records. Quantitative measures of the flow such as landing flow width, impact angle, etc. are extracted using the ImageJ software package [20].

D. Numerical method

The numerical approach developed by Wang and Desjardins [21] is employed in this work. The verified level-set computational strategy is accurate, conservative, and robust in simulating inertia dominated liquid-gas flows with moving contact lines [21, 22]. We provide a brief mathematical description of the methods here.

The liquid and gas phases are governed by the Navier-Stokes equations, written as

$$\frac{\partial \rho \mathbf{u}}{\partial t} + \nabla \cdot (\rho \mathbf{u} \otimes \mathbf{u}) = -\nabla p + \nabla \cdot \left(\mu \left[\nabla \mathbf{u} + \nabla \mathbf{u}^{\mathsf{T}}\right]\right) + \rho \mathbf{g}, \tag{13}$$

where $\mathbf{u}$ is the velocity vector, p is the pressure field, ρ is the density, μ is the dynamic viscosity, and $\mathbf{g}$ is the gravitational acceleration vector. The continuity equation with the incompressible constraint is

$$\frac{\partial \rho}{\partial t} + \nabla \cdot (\rho \mathbf{u}) = \frac{\partial \rho}{\partial t} + \mathbf{u} \cdot \nabla \rho = 0. \tag{14}$$

An Accurate Conservative Level-Set (ACLS) method [23] is employed to implicitly capture the liquid-gas interface. The level-set function is defined as a hyperbolic tangent profile written as

$$\psi(\mathbf{x}, t) = \frac{1}{2}\left(\tanh\left(\frac{\phi(\mathbf{x}, t)}{2\varepsilon}\right) + 1\right), \tag{15}$$

where ε is the thickness of the profile, set to half the grid size in this work. The standard signed distance function ϕ is written as

$$\phi(\mathbf{x}, t) = \pm \|\mathbf{x} - \mathbf{x}_\Gamma\|, \tag{16}$$

where $\mathbf{x}_\Gamma$ corresponds to the closest point from $\mathbf{x}$ on the liquid-gs interface Γ.

In the ACLS method, the interface is defined as an iso-surface of a smooth function $\psi = 0$, and is transported by solving

$$\frac{\partial \psi}{\partial t} + \nabla \cdot (\mathbf{u}\psi) = 0. \tag{17}$$

To preserve the hyperbolic tangent profile, we solve the re-initialization equation introduced by Chiodi and Desjardins [24],

$$\frac{\partial \psi}{\partial \tau} = \nabla \cdot \left[\frac{1}{4\cosh^2\left(\frac{\phi}{2\varepsilon}\right)} \left(|\nabla \phi \cdot \mathbf{n}_\Gamma| - 1 \right) \mathbf{n}_\Gamma \right], \tag{18}$$

where τ is the pseudo-time and $\mathbf{n}_\Gamma$ is the interface normal vector computed as $\mathbf{n}_\Gamma = \frac{\nabla \phi}{|\nabla \phi|}$.

The pressure discontinuity caused by surface tension is solved using the ghost fluid method of Fedkiw *et al.* [25]. The solid phase is assumed stationary. A conservative immersed boundary method based on the cut-cell method of Meyer *et al.* [26] is employed to represent the solid phase as implemented by Desjardins *et al.* [27]. The contact line model in this paper is based on a curvature boundary condition method [21] proposed originally by Luo et al. [28]. The mathematical description presented above is implemented in the framework of the NGA code [29]. The Navier-Stokes equations are solved on a staggered grid with second-order spatial accuracy for both convective and viscous terms, and by the semi-implicit Crank-Nicolson scheme with second-order accuracy for time advancement. In all of the simulations reported here, we ensure all the parameters are those of the experiments. Figure 5 shows a grid-independence study with respect to the landing width, landing length, and landing area of the unsteady jet in Fig. 6(b). Three dimensionless meshes $d_j/\Delta = 4.8, 9.6$, and 19.2 are simulated, where Δ is the mesh size. The results for $d_j/\Delta = 9.6$ and $d_j/\Delta = 19.2$ show that the dimensions of interest are nearly coincident, illustrating good convergence. We therefore employ $d_j/\Delta = 9.6$ in the simulations to minimize runtime.

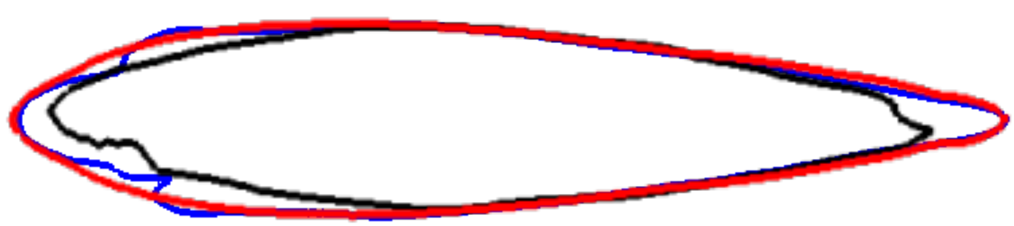

FIG. 5. Numerical convergence study for the shape of the landing area for various grid resolutions. The numerical results shown are obtained for dimensionless meshes of different resolutions: $d_j/\Delta = 4.8$(black), 9.6(blue), and 19.2(red).

V. RESULTS

Following the definitions provided by Celestini *et al.* [6], 'stable' rebounds are those where the rebounded jet profile in the near impact region is steady with no observed higher harmonic or aperiodic oscillations and no traveling waves, Fig. 6(a). Rebounding jets are 'unstable' when unsteady aperiodic oscillations, traveling waves, and premature Rayleigh breakup are observed, Fig. 6(b). If the perturbations on the bounding rims are given sufficient time to grow, the rim breaks up and splashing occurs, Fig. 6(c). The landing flow structure provides additional distinctions from which to further classify the rebound behavior. The jet rebound regimes shown in Fig. 6 are presented in the regime map of Fig. 7 in terms of Reynolds number Re and perpendicular Weber number $\mathrm{We}_{\perp}$. All data are collected from the drop tower experiments with symbol size proportional to incident jet diameter.

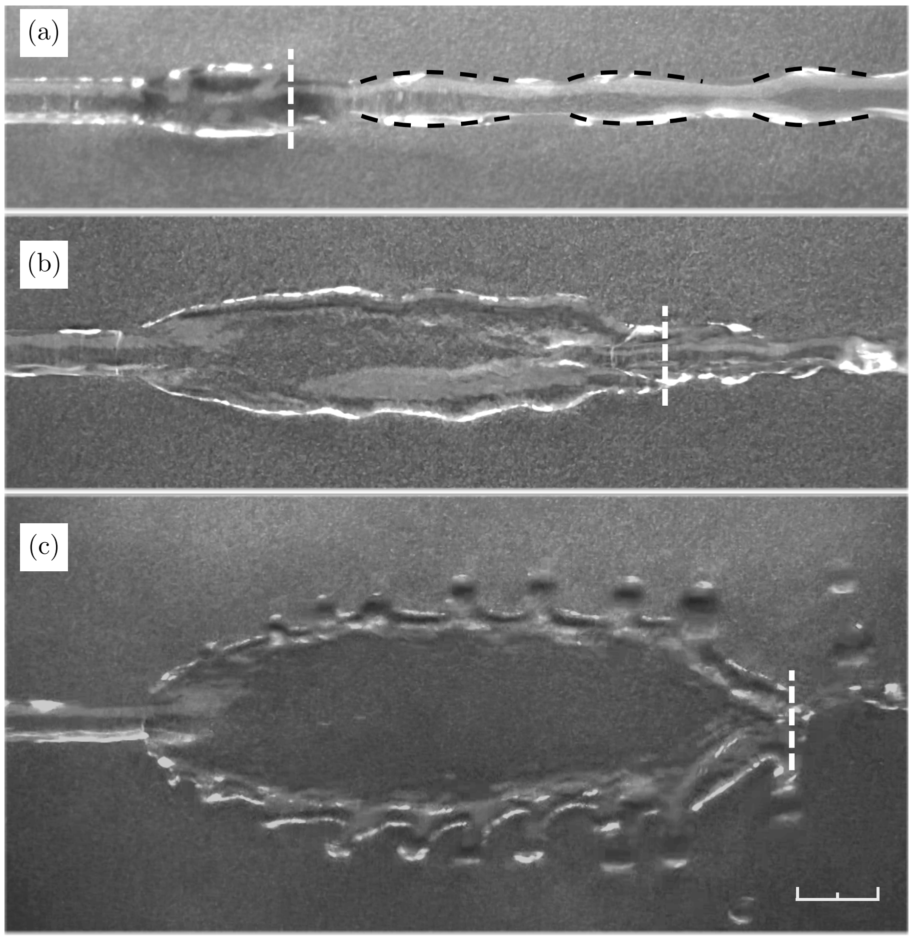

FIG. 6. Top view still images taken from drop tower test footage of oblique impacts of a water jet with a superhydrophobic ($\theta = 158°$) substrate in a nearly weightless environment. Regimes include: (a) stable, $\phi_i = 15.1°$, $\mathrm{We}_{\perp} = 1.50$ (D1), (b) unstable, $\phi_i = 18.3°$, $\mathrm{We}_{\perp} = 10.05$ (D3), and (c) fishbone, $\phi_i = 33.5°$, $\mathrm{We}_{\perp} = 37.12$ (D4). Light dashed lines indicate the location where the jet leaves the substrate. Dark dashed lines outline the stable rebounded jet profile which does not change with time. Scale bar is 1 cm.

As observed from the regime map of Fig. 7, stable rebounds occur in the lowest inertia laminar region where $\mathrm{Re} \lesssim 3000$ and $\mathrm{We}_{\perp} \lesssim 20$. The stable jet landing flow is characterized by relatively small maximum width w and equally smooth and steady bounding rims. The maximum landing flow width for stable rebounds is less than twice the initial jet diameter. Rim impact asymmetry gives rise to minor-major axis switching oscillations along the rebounded jet. As noted by Celestini *et al.* [6], the rebounding jet oscillations are similar to those present on jets generated from elliptic nozzles. Such oscillations persist until the jet breaks up downstream due to the perturbation growth.

For the low-gravity tests we readily observe stable jet rebounds at low impact angles as the jet incidence becomes parallel to the substrate. Even tangent jets that are sufficiently close to the substrate, where $\phi_i = 0$ and $\mathrm{We}_{\perp} = 0$, are observed to rebound due to the interaction of naturally increasing varicose undulation amplitudes with the substrate,

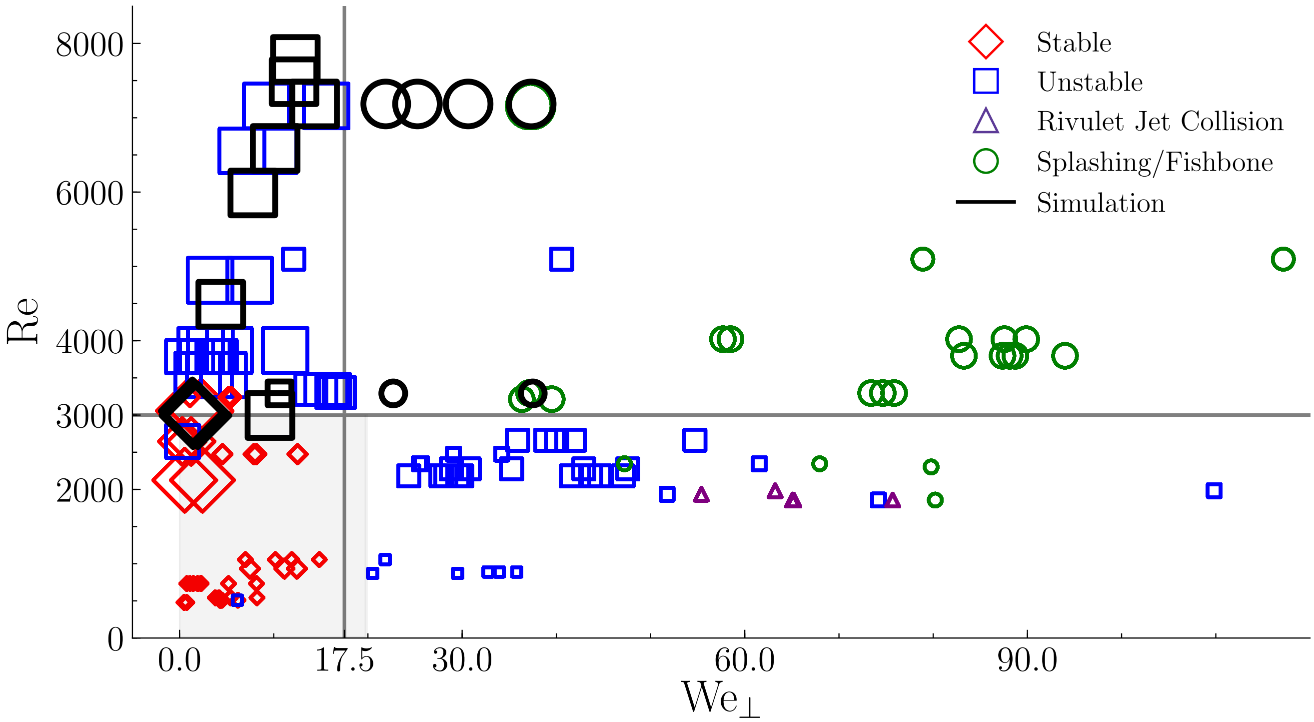

FIG. 7. Regime map illustrating the observed dependence of flow structures emerging from the oblique impact of a rebounding jet from a superhydrophobic substrate. Marker size is proportional to the diameter of the jet and black bold markers represent numerical simulations. The horizontal line at $\mathrm{Re} = 3000$ marks the approximate transition to turbulent flow for the incident jet and the vertical line at $\mathrm{We}_\perp = 17.5$ marks the predicted onset of splashing behavior (Eq. 12 with $C_1 = 1/2$. The fit coefficient $C_1 = 1/2$ is justified by Fig. 9). The shaded region represents the extent of Celestini *et al.* [6].

as demonstrated in Fig. 8. In a terrestrial environment, such a jet attaches to the substrate as a rivulet as reported by Celestini *et al.* [6]. However, in low-gravity environments, for such low incident angle impacts $\mathrm{We}_\perp$ is not determined by jet velocity but by free jet perturbation growth rates which are essentially normal to the jet axis. Since such perturbations grow with velocities $v_p \sim (\sigma/\rho d_j)^{1/2}$, we find an effective perpendicular Weber number, based on the growth velocity v_p of $\mathrm{We}_p \sim 1$, which lies within the stable rebound regime observed in the experiments when $\mathrm{Re} \lesssim 3000$. If the jet rebounds from the substrate with velocity v_p, the jet rebound angle can by approximated by

$$\phi_r \sim \tan^{-1}\left[\frac{v_p}{v}\right] = \tan^{-1}\left[\left(\frac{1}{\mathrm{We}}\right)^{1/2}\right]. \tag{19}$$

Using a small angle expansion Eq. 19 yields

$$\phi_r \sim \left(\frac{1}{\mathrm{We}}\right)^{1/2}. \tag{20}$$

Given the minimum Weber number for jetting of $\mathrm{We} \sim 4$ as identified by Clanet and Lasheras [30], from Eq. 19 we can expect a maximum rebound angle for a tangent jet of $\phi_r \sim 27°$.

Outside the stable regime, unsteady varicose perturbations are observed along the free surfaces of the landing flow rims and the rebounded jet. Sources of such perturbations include capillary pinching as well as higher frequency oscillations from fluctuations naturally present in the incoming jet. The perturbations continue beyond the rim impact point and are present on the rebounding jet. Unstable regimes exhibit increased normalized landing flow widths of $1.5 \leq w/d_j \leq 9$ as determined using time average composite images of the mean of each pixel for all frames captured during the low-gravity portion of the drop tower tests.

The normalized landing flow width ratio w/d_j is plotted against $\mathrm{We}_\perp$ in Fig. 9, where an increasing, somewhat monotonic, dependence is observed.

As $\mathrm{We}_\perp$ increases the combination of rim capillary pinching and the radial flow extrudes ligaments that ultimately pinch off as droplets. The droplet formation is periodic and symmetric across the flow centerline. Droplets that detach from the rim also detach from the substrate. Splashing regimes exhibit normalized landing flow widths of $5 \leq w/d_j \leq 10$. The landing flow width prediction Eq. 9 with $C_1 = 1/2$ over-predicts for the splashing regime at high $\mathrm{We}_\perp$, Fig. 9. This decreased landing flow width can be attributed to the mass lost from the rim as ejected droplets as discusses in Bremond and Villermaux [11].

As shown in Fig. 7, an 'island' of unique behavior arises for laminar jets when $\mathrm{Re} \approx 2000$ and $8 \lesssim \mathrm{We}_\perp \lesssim 50$. In this regime the landing flow forms a terminal third rim at its downstream edge which redirects fluid towards the converging outer rims as shown in Fig. 10. A time averaged composite image and sketch of such a landing flow are presented in Fig. 10(a). The two rim rivulets and terminal third rim are sketched in Fig. 10(b). Both outer rim rivulets rebound from the substrate as half-volume jets at the intersection of the primary rivulet rims and the terminal rim. The two rebounding jets then take convergent paths, colliding and coalescing to form a single rebounded jet. The suggestion of this rebound mechanism is supported by the slight rim angle change α at the point of rebound sketched in Fig. 10(a).

As the impact angle approaches a normal impingement, the Weber number of the secondary jet reduces drastically compared to the incoming jet, which results in a flow that may be described more accurately as an attached bulbous blob rather than a jet, as shown in Fig 11. Thus, the rebounded jet acts more like 'dripping' flow from a nozzle as opposed to jetting from one. Below a critical Weber number the flow inertia in the secondary jet is not sufficient to induce jetting and may result in periodic large droplet detachments or the growth of a large attached body of fluid. In 1-g_o the landing flow simply feeds into a large puddle, Fig. 11(a); a drastically different outcome from what is observed in low-g.

For the high contact angles and minimal hysteresis in the experiments, the simulations are able to quantitatively capture features of the landing flow. For both stable and unstable regimes, the qualitative appearance and characteristic landing flow dimensions are captured by the numerical simulations, Fig. 12(a,b). Splashing regime simulations capture the obvious flow features of rim destabilization and droplet ejection, Fig. 12(c). As shown in Fig. 7, simulations agree with the determined regime boundaries. The simulations performed at $\mathrm{Re} \approx 7000$ support the critical weber number of $\mathrm{We}_\perp \approx 17.5$. Landing flow widths determined from simulations are included in Fig. 9 and show agreement across all regimes.

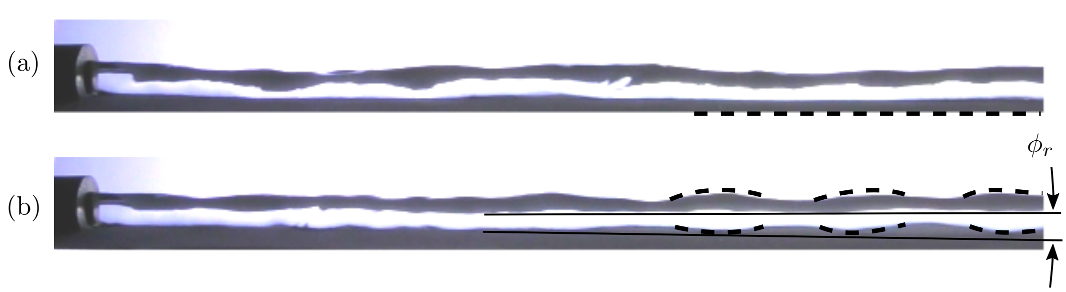

FIG. 8. Still images of a tangent jet taken from drop tower test footage in (a)1-g before the drop and (b) low-g following the drop package release. In 1-g the jet attaches to the substrate and advances as a rivulet (dashed line). In low-g the growing varicose perturbations deflect the jet away from the substrate (dashed curved segments). The downstream jet in (b) is not in contact with the substrate.

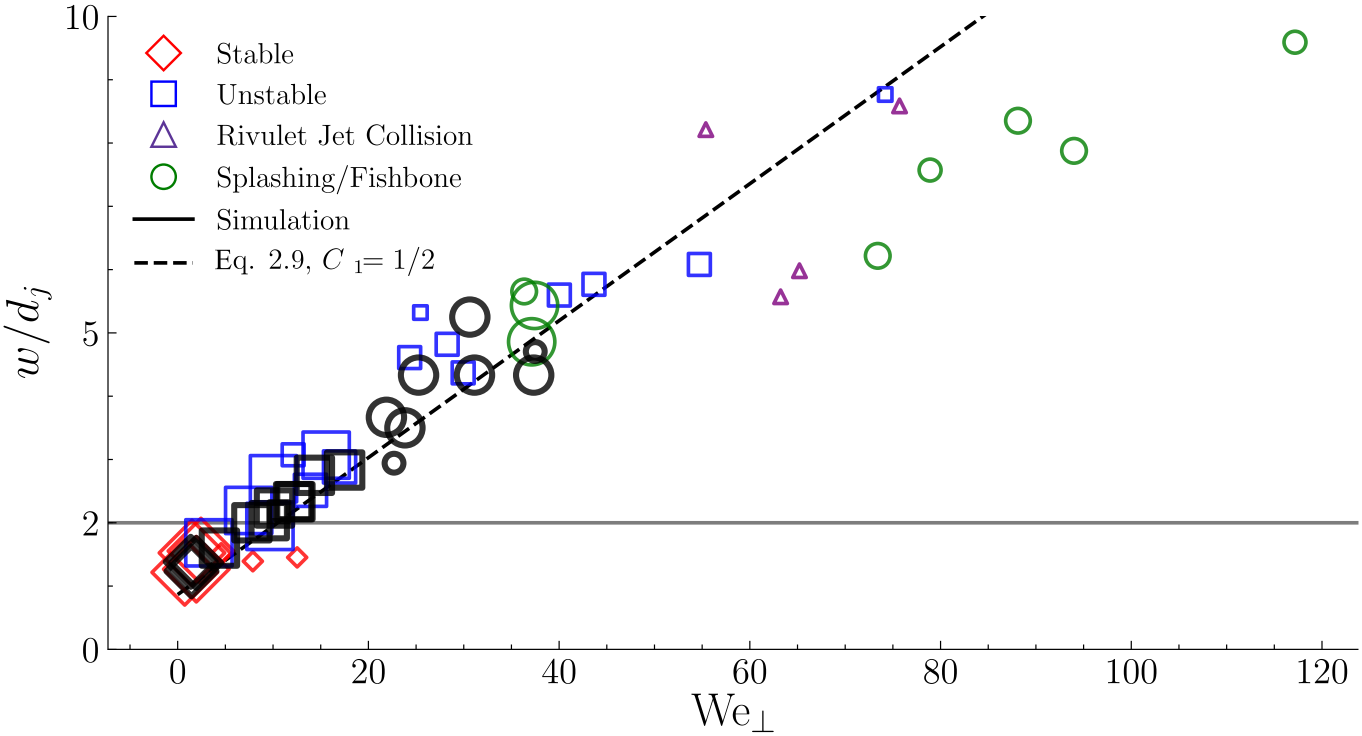

FIG. 9. Normalized landing flow width w/d_j as a function of $\mathrm{We}_\perp$. Gray line indicates a maximum normalized landing flow width of $w/d_j \sim 2$ for stable rebounds. Marker size is proportional to d_j and black bold markers represent simulations.

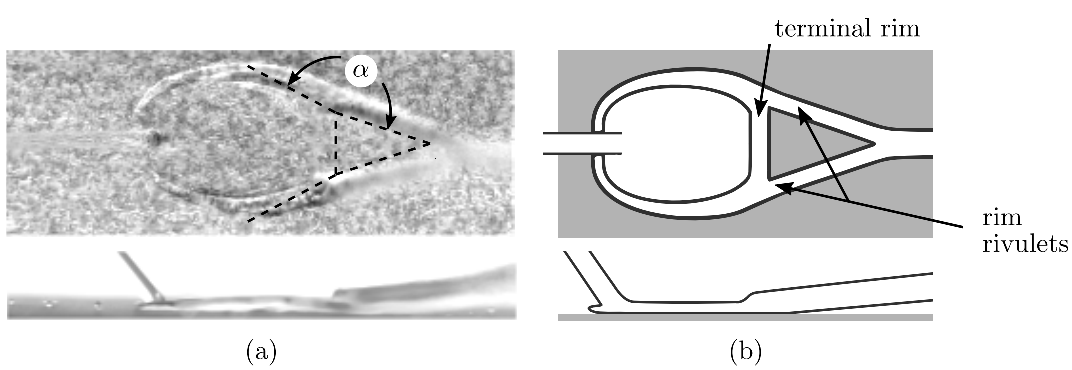

FIG. 10. (a) Top and profile views of time-averaged composite image and (b) sketch of the landing region for the double rivulet jet collision regime (D5). The landing flow film splits producing a third 'terminal rim'. The two edge rivulets rebound from the substrate at the point of intersection with the terminal rim only to collide and coalesce downstream forming a single rebounding jet. The triangular void in the flow observed from above is outlined with a dashed line in (a).

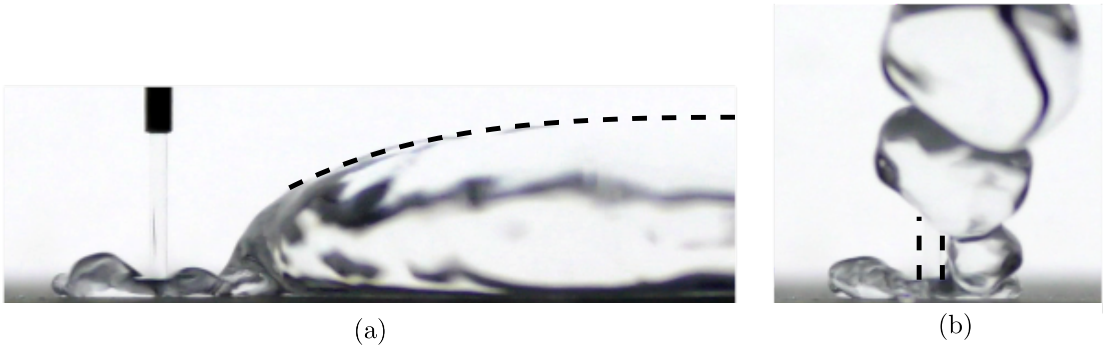

FIG. 11. Still images taken from drop tower test footage of a normal jet impingement in 1-g (a) before the drop and low-g (b) after the drop package release. In 1-g the fluid leaving the downstream edge of the landing flow feeds a puddle of height $\sim 2l_c$. In low-g a low Weber number 'jet' is formed which may exhibit dripping behavior, emitting large droplets, and producing a large attached blob. Large attached blob (a) and incoming jet (b) are outlined with a dashed black line.

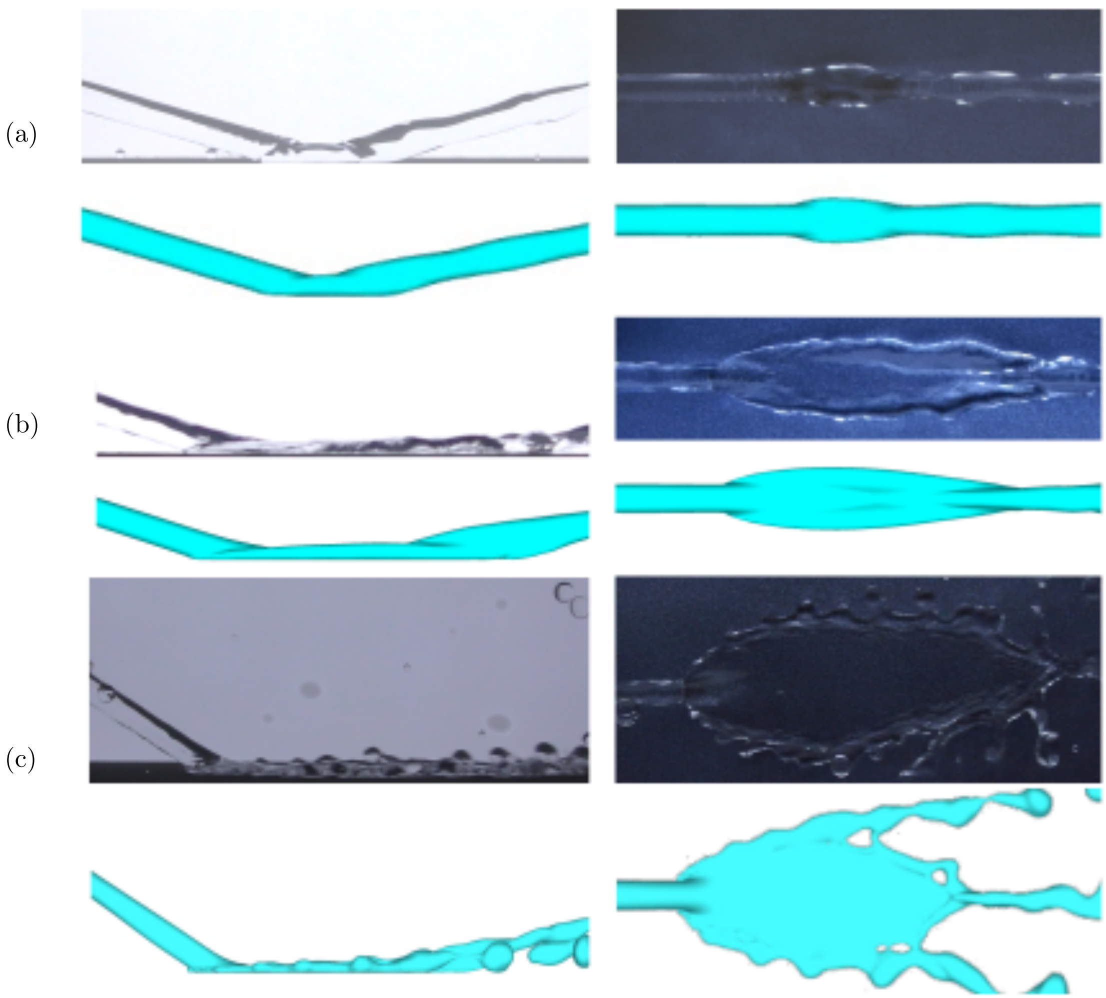

FIG. 12. Profile and top view comparisons of numerics with drop tower tests for d_j=6 mm jet. Comparisons include: (a) stable, $\phi_i = 15.1°$, $\mathrm{We}_\perp = 1.50$ (D1), (b) unstable, $\phi_i = 18.3°$, $\mathrm{We}_\perp = 10.05$ (D3), and (c) fishbone, $\phi_i = 33.5°$, $\mathrm{We}_\perp = 37.12$ (D4).

VI. CONCLUSION

This work has expanded the regime map for jet rebound by an order of magnitude, spanning the stable and unstable regime, while adding new splashing/fishbone and double rivulet jet collision regimes. The double rivulet jet collision regime has not been previously reported in papers on jet rebound phenomena. We demonstrate that there is no low-g low-angle limit for jet rebound; i.e., even tangent jets rebound. When the impact angle approaches 90° the rebounded jet enters a dripping regime characterized by intermittent detachment of large droplets or a large fluid body that remains attached to the landing flow.

The energy model we develop predicts the landing flow dimensions as a function of the perpendicular Weber number $\mathrm{We}_\perp$, Eq. 9. The landing flow width is predicted with an error of $\pm 1.1 d_j$. Using the predicted landing flow dimensions in conjunction with models for the rim residence time τ_r and rim capillary pinching time τ_p we determined a critical Weber number $\mathrm{We}_\perp$ for splashing, Eq. 12. Additional scaling laws are derived for the maximum angle of a tangent jet rebound and the rim convergence angle.

During jet impact the fluid is subjected to an effective acceleration of $a \sim v_\perp^2/D$. For rebound to occur $\mathrm{Bo}_a/\mathrm{Bo} = v_\perp^2/d_j g > 1$ where Bo_a is the Bond number based on the acceleration of impact. The transition from the impact shape to a static equilibrium geometry gives rise to the jet rebound. For the jet to rebound we expect $\mathrm{Bo} \sim 1$; therefore, we expect a minimum perpendicular velocity for terrestrial rebound of $v_\perp \sim (\sigma/\rho d_j)^{1/2}$, below which rebound will not occur in a terrestrial environment.

Level set numerical simulations capture the landing flow regimes and geometry across the investigated parameter range. The simulations in the splashing region capture the rim destabilization but fail to capture the general flow structure, especially after the point of maximum width. Given the accuracy of the code it would now be prudent to investigate rebounds that cannot be captured in 1-g or drop tower tests.

With a view towards future work, there are many interesting and unaddressed questions remaining. For example, the characteristics of splashing such as the detached droplet size and distribution are left to follow-on studies. Recently, Kibar [31] studied jet rebound from a convex substrate but rebound from a concave substrate remains unstudied. The obvious effect of a concave substrate is that the curvature would act to suppress jet rebound as shown in Fig. 13. The additional dissipation associated with viscous fluids and lower contact angles is also a rich direction for investigation. A viscous fluid would slow the growth of perturbations that cause rim pinching and splashing. Near-normal impacts and the transition of the rebounded jet from dripping to jetting could be investigated. Near-normal impacts, viscous impacts, and varying surface wettability could all be supported readily by additional simulations.

FIG. 13. Images from drop tower tests showing the impact of a liquid jet with a concave superhydrophobic substrate. The jet velocity increases from left to right increasing the intact length of the rivulet. The curvature of the substrate suppresses the rebound of the jet. Dashed lines show the rivulet intact length.

[1] E. J. Watson, The radial spread of a liquid jet over a horizontal plane, Journal of Fluid Mechanics **20**, 481 (1964).

[2] R. P. Kate, P. K. Das, and S. Chakraborty, Hydraulic jumps due to oblique impingement of circular liquid jets on a flat horizontal surface, Journal of Fluid Mechanics **573**, 247 (2007), first.
[3] R. P. Kate, P. K. Das, and S. Chakraborty, Hydraulic jumps with corners due to obliquely inclined circular liquid jets, Physical Review E **75**, 10.1103/physreve.75.056310 (2007), second.
[4] C. Ellegaard, A. E. Hansen, A. Haaning, K. Hansen, A. Marcussen, T. Bohr, J. L. Hansen, and S. Watanabe, Cover illustration: Polygonal hydraulic jumps, Nonlinearity (1999).
[5] E. Dressaire, L. Courbin, J. Crest, and H. A. Stone, Thin-film fluid flows over microdecorated surfaces: Observation of polygonal hydraulic jumps, Physical Review Letters **102**, 10.1103/physrevlett.102.194503 (2009).
[6] F. Celestini, R. Kofman, X. Noblin, and M. Pellegrin, Water jet rebounds on hydrophobic surfaces: a first step to jet micro-fluidics, Soft Matter **6**, 5872 (2010).
[7] A. Kibar, H. Karabay, K. S. Yiğit, I. O. Ucar, and H. Y. Erbil, Experimental investigation of inclined liquid water jet flow onto vertically located superhydrophobic surfaces, Experiments in Fluids **49**, 1135 (2010).
[8] A. Kibar, Experimental and numerical investigations of the impingement of an oblique liquid jet onto a superhydrophobic surface: energy transformation, Fluid Dynamics Research **48**, 015501 (2015).
[9] J. W. M. Bush and A. E. Hasha, On the collision of laminar jets: fluid chains and fishbones, Journal of Fluid Mechanics **511**, 285 (2004).
[10] N. Ashgriz, *Handbook of Atomization and Sprays*, edited by N. Ashgriz (Springer US, 2011).
[11] N. Bremond and E. Villermaux, Atomization by jet impact, Journal of Fluid Mechanics **549**, 273 (2006).
[12] G. Taylor, The dynamics of thin sheets of fluid. III. disintegration of fluid sheets, Proceedings of the Royal Society A: Mathematical, Physical and Engineering Sciences **253**, 313 (1959).
[13] F. E. C. Culick, Comments on a ruptured soap film, Journal of Applied Physics **31**, 1128 (1960).
[14] J. Eggers and E. Villermaux, Physics of liquid jets, Reports on Progress in Physics **71**, 036601 (2008).
[15] A. B. D. Cassie and S. Baxter, Wettability of porous surfaces, Transactions of the Faraday Society **40**, 546 (1944).
[16] S. Kaps, R. Adelung, M. Scharnberg, F. Faupel, S. Milenkovic, and A. W. Hassel, Determining superhydrophobic surfaces from an expanded cassie baxter equation describing simple wettability experiments, arXiv preprint arXiv:1408.5273 (2014).
[17] A. P. Wollman, *Capillarity-driven Droplet Ejection*, Master's thesis, Portland State University (2012).
[18] K. A. Brakke, The surface evolver, Experimental Mathematics **1**, 141 (1992).
[19] Y. Chen, B. Schaffer, M. Weislogel, and G. Zimmerli, Introducing SE-FIT: Surface evolver - fluid interface tool for studying capillary surfaces, in *49th AIAA Aerospace Sciences Meeting including the New Horizons Forum and Aerospace Exposition* (American Institute of Aeronautics and Astronautics, 2011).
[20] J. Schindelin, I. Arganda-Carreras, E. Frise, V. Kaynig, M. Longair, T. Pietzsch, S. Preibisch, C. Rueden, S. Saalfeld, B. Schmid, J.-Y. Tinevez, D. J. White, V. Hartenstein, K. Eliceiri, P. Tomancak, and A. Cardona, Fiji: an open-source platform for biological-image analysis, Nature Methods **9**, 676 (2012).
[21] S. Wang and O. Desjardins, 3D numerical study of large-scale two-phase flows with contact lines and application to drop detachment from a horizontal fiber, International Journal of Multiphase Flow **101**, 35 (2018).
[22] S. Wang and O. Desjardins, Numerical study of the critical drop size on a thin horizontal fiber: Effect of fiber shape and contact angle, Chemical Engineering Science **187**, 127 (2018).
[23] O. Desjardins, V. Moureau, and H. Pitsch, An accurate conservative level set/ghost fluid method for simulating turbulent atomization, Journal of Computational Physics **227**, 8395 (2008).
[24] R. Chiodi and O. Desjardins, A reformulation of the conservative level set reinitialization equation for accurate and robust simulation of complex multiphase flows, Journal of Computational Physics **229**, 6300 (2016).
[25] R. P. Fedkiw, T. Aslam, B. Merriman, and S. Osher, A non-oscillatory eulerian approach to interfaces in multimaterial flows (the ghost fluid method), Journal of Computational Physics **152**, 457 (1999).
[26] M. Meyer, A. Devesa, S. Hickel, X. Hu, and N. Adams, A conservative immersed interface method for large-eddy simulation of incompressible flows, Journal of Computational Physics **229**, 6300 (2010).
[27] O. Desjardins, J. McCaslin, M. Owkes, and P. Brady, Direct numerical and large-eddy simulation of primary atomization in complex geometries, Atomization and Sprays **23**, 1001 (2013).
[28] J. Luo, X. Hu, and N. Adams, Curvature boundary condition for a moving contact line, Journal of Computational Physics **310**, 329 (2016).
[29] O. Desjardins, G. Blanquart, G. Balarac, and H. Pitsch, High order conservative finite difference scheme for variable density low mach number turbulent flows, Journal of Computational Physics **227**, 7125 (2008).
[30] C. Clanet and J. C. Lasheras, Transition from dripping to jetting, Journal of Fluid Mechanics **383**, 307 (1999).
[31] A. Kibar, Experimental and numerical investigation of liquid jet impingement on superhydrophobic and hydrophobic convex surfaces, Fluid Dynamics Research **49**, 015502 (2016).